CrossMark

JFM PAPERS

Effects of an along-shelf current on the generation of internal tides near the critical latitude

Yangxin He[1],† **and Kevin G. Lamb**[1],†

[1]Department of Applied Math, University of Waterloo, Waterloo, ON N2L 3G1, Canada

The effects of along-shelf barotropic geostrophic currents on internal wave generation by the K_1 tide interacting with a shelf at near-critical latitudes are investigated. The horizontal shear of the background current results in a spatially varying effective Coriolis frequency which modifies the slope criticality and potentially creates blocking regions where freely propagating internal tides cannot exist. This paper is focused on the barotropic to baroclinic energy conversion rate, which is affected by a combination of three factors: slope criticality, size and location of the blocking region where the conversion rate is extremely small and the internal tide (IT) beam patterns. All of these are sensitive to the current parameters. In our parameter space, the current can increase the conversion rate up to 10 times.

1. Introduction

Studies on internal tides (ITs) have attracted considerable attention over the years, because these waves can have a significant impact on oceanic mixing (Munk & Wunsch 1998; Vic *et al.* 2019), large scale ocean circulation (Wunsch & Ferrari 2004), transport of energy (Simmons & Alford 2012), upwelling of nutrients (Schafstall *et al.* 2010) and shaping the continental shelves (Cacchione, Pratson & Ogston 2002). *In situ* observations suggest that strong mixing occurs over rough bathymetry (Polzin *et al.* 1997), the biweekly variation of the mixing indicating a relationship to the spring-neap barotropic tidal cycle and thus to the conversion of barotropic to baroclinic tidal energy. The most prominent IT generation mechanism is barotropic tidal flows incident upon bottom topography such as the continental shelf slope, subsurface ridges and seamounts. Examples of generation locations include the Bay of Biscay (New & Pingree 1992; Gerkema, Lam

† Email addresses for correspondence: y67he@uwaterloo.ca, kglamb@uwaterloo.ca

& Maas 2004), the Australian North West Shelf (Holloway, Chatwin & Craig 2001), the Malin–Hebrides Shelf (Xing & Davies 1998), the Hawaiian Ridge (Martin, Rudnick & Pinkel 2006), Mid-Atlantic Ridge (Zilberman *et al.* 2009), Monterey Bay (Lien & Gregg 2001) and various seamounts (Lueck & Mudge 1997; Toole *et al.* 1997). Global numerical simulations (Simmons, Hallberg & Arbic 2004; Niwa & Hibiya 2011) have been conducted to investigate the spatial distribution of the major generation sites. They found that the generation of baroclinic tides largely occurs over prominent topographic features and the total conversion rate increases as the model grid spacing is reduced.

There are three important dimensionless parameters relevant to internal waves (IWs) generated by tide–topography interaction. The first one is the tidal excursion parameter ϵ, which is used to measure the nonlinearity of the waves (Vlasenko, Stashchuk & Hutter 2005; Legg & Huijts 2006; Garrett & Kunze 2007). It is defined as the ratio of the barotropic tidal advection distance to the horizontal scale of the topography. If ϵ is much smaller than 1, linear ITs are generated mainly at the forcing frequency. The second dimensionless parameter is the relative height of the topography $\delta = h/H$, where h is the topographic height and H is a typical water depth. The third important parameter for IT generation is the bottom slope criticality $\alpha = s/\gamma$, where s is the topographic slope and γ is the slope of an IT characteristic. In the presence of a barotropic background flow $V(x)$ in the y-direction, which varies slowly in the x-direction so that second-order gradients are negligible, under the hydrostatic approximation,

$$\gamma = \sqrt{\frac{\sigma_T^2 - f_{eff}^2}{N^2}}. \tag{1.1}$$

Here $f_{eff}^2 = f^2 + f V_x$ is the effective Coriolis frequency squared (Mooers 1975), σ_T is the IT frequency and N is the buoyancy frequency. In general, N is a function of z and γ can depend on both x and z.

The critical latitude is defined as the latitude where $f = \sigma_T$ for each tidal constituent. Critical latitudes are approximately $30°$ and $75°$ for the diurnal K_1 and semi-diurnal M_2 tides, respectively. Note that (1.1) is not valid if $f_{eff} > \sigma_T$. Instead we have an evanescent region, where no freely propagating waves are permitted and forced waves decay quasi-exponentially away from the generation site. If the length of the evanescent region is finite, meaning f_{eff} varies spatially, a fraction of the wave energy can tunnel through the region and there is a radiated wave on the other side of the region. Intensive research on tunnelling has been done with most of it focused on vertically propagating waves in the atmospheric context (Jones 1970; Monserrat & Thorpe 1996; Sutherland & Yewchuk 2004), though some work has discussed tunnelling in the ocean (Eckart 1961; Rainville & Pinkel 2004).

Unlike numerical studies, the theoretical models all use linearized equations of motion and most of them are formulated without a background current, i.e. $f_{eff} = f$. When α is much less than 1, the analysis of Bell (1975) has been widely used for small amplitude bathymetry $\delta \ll 1$. Bell included the advection by the background flow and used an infinitely deep ocean to estimate the upward energy flux for subcritical topography to be $O(1) \, \text{mW m}^{-2}$. Building upon Bell's work, Khatiwala (2003) included a rigid lid, which results in horizontal, rather than vertical, energy flux. He found good agreement with that predicted by a nonlinear numerical model. Llewellyn Smith & Young (2002) too present an analytical treatment of this problem by using a different mathematical approach (WKB method) to include non-uniform $N(z)$. While most models with small bathymetry $\delta \ll 1$ use a linearized bottom boundary condition, St. Laurent & Garrett (2002) used a

perturbation expansion of the bottom boundary condition for small but finite amplitude topography. However, the linear theory in general underestimates the energy flux for supercritical cases.

Bathymetries with large amplitudes have also been considered theoretically. In this case, the bottom boundary condition cannot be linearized. For subcritical slopes with $\alpha < 1$, the model developed by Baines (1982) is available. Craig (1987) used the method of characteristics and described the generation of ITs of a single frequency at shelf-like topography with a constant shelf slope. He found that energy flux varies linearly with α and like α^5 for supercritical and subcritical cases, respectively. Similar results for subcritical cases were obtained by Vlasenko *et al.* (2005). Balmforth, Ierley & Young (2002) considered an infinitely deep ocean, while a finite depth ocean was discussed by St. Laurent *et al.* (2003) with a finite amplitude knife edge, step-like and top hat bathymetry. This work was extended by Nycander (2006), where he considered periodic knife edge bathymetry. Pétrélis, Smith & Young (2006) applied a Green's function to large submarine ridges assuming small tidal excursion distance ϵ. Their results confirm a monotonic increase in the radiated energy flux as the slope becomes steeper, with most of the increase happening after the slope becomes slightly supercritical. Other models include those of Gerkema (2002), Gerkema *et al.* (2004) and Baines (1973). However, none of these models on large amplitude bathymetries include advection by the barotropic tide and they generally need to be solved numerically owing to the model complexity. Therefore, they are restricted to small tidal excursions.

Numerical simulations using primitive equation models to study IT generation by tide–topography interaction have become increasingly important particularly for regions where linear theories break down or become complex. Legg & Huijts (2006) used a Gaussian ridge to confirm that strong local mixing only occurs for narrow features with large α, which is common in the coastal ocean. Holloway & Merrifield (1999) and Munroe & Lamb (2005) focused on idealized seamounts and showed that large seamounts are ineffective at generating ITs unless they are elongated in a direction normal to the barotropic tides. The aforementioned papers all used free surface in their models, while Lamb & Kim (2012) applied a rigid lid and concluded that the large amplitude theory yields good results with simulations using subcritical slopes. Investigations of IT generation using more realistic bathymetries are numerous, e.g. Powell *et al.* (2012), Niwa & Hibiya (2004, 2014), Merrifield, Holloway & Johnston (2001), Holloway (1996) and Zilberman *et al.* (2009). More details on the theories and numerical simulations can be found in the review by Garrett & Kunze (2007).

Most of the aforementioned research is relatively basic in the sense that only the effect of barotropic tides and bathymetry is considered in the IW generation process. This paper builds on past work by investigating IT generation over a shelf in the presence of an along-shelf geostrophic current, which is a common feature along continental shelves. Strong oceanic currents, such as the Gulf Stream, Kuroshio, Oyasio, the Pacific Equatorial Countercurrent and Davidson Current are a significant source of mass, heat and nutrient transport in the world's oceans (Hall & Bryden 1982). The presence of the currents can significantly modify the background density, effective frequencies and velocity field, which in turn modulates the IW field including its propagation path, energy distribution and generation process. Incorporating geostrophic currents into studies of IW generation is necessary and our knowledge is far from complete. One of the first theoretical studies of IWs propagating into a geostrophic current dates back to Mooers (1975), who investigated two-dimensional IWs normally incident on a frontal zone using the method of characteristics. Kunze (1985) extended Mooers' work to a three-dimensional

setting by considering the influence of mean flow shear on wind generated near-inertial waves (NIWs). Since then, research on the impact of currents on ITs, particularly through variations in wave frequency, is still sparse and largely focused on linear equations/theories and some observations (Chuang & Wang 1981; Kolomoitseva & Cherkesov 1999; Rainville & Pinkel 2006; Chavanne *et al.* 2010; Whitt & Thomas 2013; Li *et al.* 2019). Richet, Muller & Chomaz (2017) investigated the impacts of a weak background current on the local dissipation of high mode IWs using fully nonlinear numerical simulations. Their currents flowed in the same direction as the waves so the wave frequency is affected owing to the Doppler shift. Dong *et al.* (2019) found that a mesoscale eddy over a seamount broadened the range of critical latitude effects and enhanced energy transfer from diurnal frequencies to higher frequencies and from low- to high-mode waves. The effects of horizontal density variability on the IT wave field with no change in f_{eff} has also been investigated (Vlasenko *et al.* 2005; Kurapov, Allen & Egbert 2010).

This paper contributes to the understanding of IT generation by including along-shelf barotropic geostrophic currents. Barotropic currents are used because this is the simplest way to study the effects of horizontal shear of the background current giving horizontally varying f_{eff} without additional complications of horizontally varying stratification. We restrict our attention to K_1 diurnal tides and near-critical latitudes so that the impact of varying V_x can be significant. The focus is on the barotropic to baroclinic energy conversion rate and the IT beam pattern. The numerical model set-up and parameter space are presented in § 2. The assumptions and calculations of conversion rates are discussed in § 3. Results of numerical simulations are presented in § 4. We present results for a selection of the numerical simulations we have undertaken chosen to illustrate the variety of effects that the along-shelf barotropic current can have on the wave generation process. In this paper, we focused on near-critical latitudes for which σ_T/f is too small for parametric subharmonic instability (PSI) to occur. The results are discussed and summarized in § 5.

2. Numerical model

We use the Massachusetts Institute of Technology Global Circulation Model (MITgcm; Marshall *et al.* 1997) in hydrostatic configuration. A rigid lid is applied at the surface $z = 0$. With a rigid lid and incompressibility, the volume flux is constant throughout the domain. With a free surface, the barotropic tide is a wave which would be partially reflected from the shelf slope resulting in a spatially variable maximum cross-shelf volume flux. The volume flux would also have a spatially varying phase; however, because tidal wave lengths are very long compared with the width of the shelf slope, these variations are not important in the present context (Stammer *et al.* 2014). For comparisons with observations, it would therefore be important to choose the tidal current amplitude so that currents at the generation site matched with the observed currents as closely as possible. Rigid lid simulations are attractive owing to the accompanied cheap computational cost, both because using a free surface is more computationally expensive and because the simulations would be much longer to allow time for the tidal waves to propagate from the boundary to the shelf slope.

The bottom is at $z = h(x)$, which is modelled as a linear slope with smoothed corners:

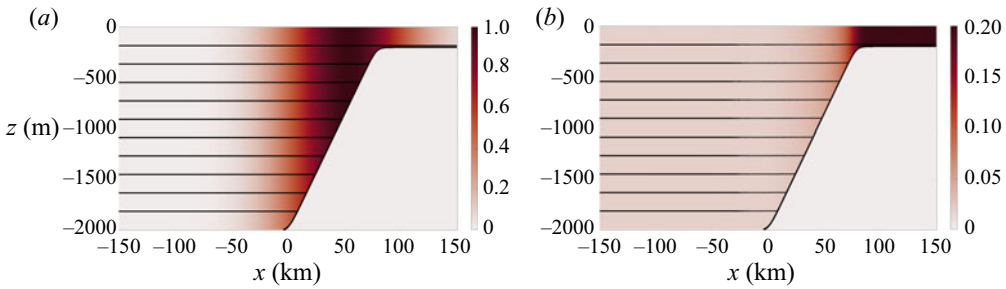$$h(x) = -H + \frac{s}{2}\left(f(x, 0, d) - f\left(x, \frac{1800}{s}, d\right)\right), \tag{2.1}$$

Figure 1. An example of the initial velocity fields (shaded) overlaid with density contours. (*a*) The initial along-shelf velocity $v(x, z, 0) = V(x)$ with $V_{max} = 1\,\mathrm{m\,s^{-1}}$, $x_0 = 50\,\mathrm{km}$ and $x_r = 60\,\mathrm{km}$. The barotropic tidal current is initially zero. (*b*) The initial cross-shelf current u, which is equal to the maximum on-shelf barotropic current. Here $A = 0.02$ in the deep water.

where

$$f(x, a, s) = x - a + s \left(\ln \left(\cosh \left(\frac{x - a}{s} \right) \right) \right). \tag{2.2}$$

The bottom of the shelf slope starts at approximately $x = 0$. Here, s is the slope of the bathymetry except near the shelf break and the bottom, where it is smoothed out by the parameter $d = 5000\,\mathrm{m}$. We use a Gaussian function to model the barotropic current,

$$V(x) = V_{max} \exp \left(-\frac{(x - x_0)^2}{x_r^2} \right). \tag{2.3}$$

Here, x_0 and x_r determine the location and width of the current and V_{max} is the maximum current velocity which occurs at its centre. This current is in geostrophic balance with a cross-shelf pressure gradient and because the current is barotropic, a horizontal density gradient is not required.

We start the simulations at peak on-shelf tidal flow and hence the barotropic tidal current (vertical average of the cross-shelf current u) is $U_{bt} = -AH/h(x) \cdot \cos(\sigma_T t)$, where $A = 0.02\,\mathrm{m\,s^{-1}}$ is the deep water barotropic current, $\sigma_T \approx 7.2935 \times 10^{-5}\,\mathrm{s^{-1}}$ is the K_1 diurnal tidal frequency and $H = 2\,\mathrm{km}$ is the water depth. The initial cross-shelf velocity field is equal to the initial barotropic current. We start the simulations at the maximum on-shelf flow because, at this time, isopycnals are close to their mean position (starting at the beginning of on-shelf flow, for example, fluid over the shelf would be raised during the first half of the tidal period and lowered in the second half and fluid parcels would have a mean position above their initial location). Starting at this phase of the tide also means that the along-shelf component of the barotropic current is zero in regions of constant depth. Thus, we initialize the along-shelf velocity field with the geostrophic current $v(x, z, 0) = V(x)$. The simulations are forced by specifying the tidal currents at the left and right boundaries. For simplicity, we consider linear stratifications with constant buoyancy frequency $N = 1 \times 10^{-3}\,\mathrm{s^{-1}}$. An example of the initial state is plotted in figure 1.

f (s^{-1})	γ (no current)	s	V_{max} (m s^{-1})	x_0 (km)	x_r (km)
6.7×10^{-5}	0.029	0.023	[−1, 1]	[−60, 180]	[40, 160]
6.0×10^{-5}	0.041	0.033	[−1, 1]	[13, 43]	[15, 60]

Table 1. Parameter space.

The parameters that can be varied under this setting are:

$$
\left.
\begin{aligned}
f : \quad & \textit{the Coriolis parameter;} \\
s : \quad & \textit{the slope of the bathymetry;} \\
x_0 : \quad & \textit{the location of the center of the current;} \\
V_{max} : \quad & \textit{the velocity of the geostrophic current at } x = x_0; \\
x_r : \quad & \textit{the width of the current.}
\end{aligned}
\right\}
\qquad (2.4)
$$

We consider bathymetries with slope s so that in the absence of a current, the slope criticality $\alpha = s/\gamma \approx 0.8$. Our setting of the geostrophic current implies the Rossby number $Ro = O(V_x/f) = O(0.1)$. The values of the relevant parameters are listed in table 1. We choose these parameters to represent real world ocean currents. For example, the current width is modelled by $4x_r$. In the Northern Hemisphere, negative V_{max} can represent western boundary currents flowing north or eastern boundary currents flowing south. Western boundary currents are generally faster and narrower than eastern boundary currents. The Gulf Stream has an average speed of 1.8 m s^{-1} and a typical width of 100 km. The mean speed of the southward flowing California current is 0.1 m s^{-1} and its width is between 500 and 800 km. However, positive V_{max} can represent western boundary currents flowing south or eastern boundary currents flowing north. The southward flowing Labrador Current has a typical speed of approximately 0.4 m s^{-1} and it is approximately 100 km wide. Speeds of the northward flowing Norwegian Coastal Current can vary greatly from 0.1 m s^{-1} to 1 m s^{-1} depending on the season. These large ranges of V_{max} and x_r are covered in our choice of parameters. We vary the current centre x_0 to model the different locations of the current relative to the bathymetry. In particular, because the focus of this paper is on near-critical latitudes, a larger parameter space was done with $f = 6.7 \times 10^{-5}$ s^{-1} ($\approx 27.5\,°$N) than that with $f = 6.0 \times 10^{-5}$ s^{-1} ($\approx 24.5\,°$N).

The central domain of interest has a length $L = 200$ km with uniform resolution d$x = 25$ m. The vertical grid is non-uniform with a total of $nz = 400$ points, in which 80 points are in the shallow water. The finest resolution is d$z = 2.5$ m in the upper 200 m and it linearly stretches to d$z = 8$ m in the deep water. On either side of the central domain, there is a layer in which the grid is slowly stretched horizontally with successive grid cell lengths increased by 0.5 %. Each simulation is run for 60 tidal periods. The total domain is long enough so that no ITs can reach the boundaries within the simulation time. The model time step is 6 s.

The horizontal viscosity is parametrized with a nonlinear Smagorinsky scheme (Smagorinsky 1993) with viscC2Smag = 2. We use PP81 to model the vertical viscosity μ and diffusivity κ (Pacanowski & Philander 1981; Stashchuk *et al.* 2017).

3. Calculation of conversion rate

To calculate the barotropic to baroclinic conversion rate, the velocity, density and pressure fields are first separated into barotropic and baroclinic fields following Kang & Fringer (2012). The total flow field is divided into

$$\boldsymbol{u} = (u, v, w) = (U_{bt} + u', V_{bt} + V + v', W_{bt} + w'), \tag{3.1}$$

$$\rho = \rho_b(z) + \rho'(x, z, t), \tag{3.2}$$

$$p = p_b(z) + p_g(x) + p_{bt}(x, z, t) + p'(x, z, t), \tag{3.3}$$

where $\boldsymbol{U}_{bt} = (U_{bt}, V_{bt}, W_{bt})$ is the velocity field associated with the barotropic tidal currents and $\boldsymbol{u}' = (u', v', w')$ is the perturbation velocity. Using an overbar above a quantity ϕ refers to the depth integral $\bar{\phi} = \int_{-h}^{0} \phi \, dz$, the barotropic current is defined as

$$U_{bt}(x, t) = \frac{1}{h(x)} \bar{u}, \tag{3.4}$$

$$V_{bt}(x, t) = \frac{1}{h(x)} \bar{v}, \tag{3.5}$$

$$W_{bt}(x, z, t) = -\frac{\partial U_{bt}}{\partial x} z. \tag{3.6}$$

Here, $\rho_b(z)$ is the background density field in hydrostatic balance with $p_b(z)$. We take $p_b = 0$ at the surface. The $p_g(x)$, given by $\partial p_g / \partial x = f V$, is the pressure associated with the geostrophic current V. We take $p_g = 0$ to the left of the current. Here, $\rho'(x, z, t)$ is the density perturbation in hydrostatic balance with $p_{bt} + p'$, where p_{bt} and p' are the barotropic and baroclinic pressure, respectively. We assume p' has zero depth average (Kunze *et al.* 2002), i.e. $p' = (p - p_b) - 1/h(x)\overline{(p - p_b)}$, and ρ' is assumed to be the baroclinic density perturbation.

The total barotropic-to-baroclinic energy conversion is given by $C = \iint \rho' g W \, dx \, dz$. In particular, C is the horizontal integration of the conversion $\bar{C} = \int \rho' g W \, dz$. Here, $\bar{C}(x, t)$ can be either positive or negative. Positive conversion means energy is converted from barotropic to baroclinic tides, while negative conversion means energy is transferred from baroclinic to barotropic tides. We denote $C_p(t) = \Sigma_{\bar{C}>0} \bar{C} \, dx$ and $C_n(t) = \Sigma_{\bar{C}<0} \bar{C} \, dx$. The summation is over all grid columns and multiplied by the horizontal spacing dx. All the values of the conversion rate are averaged over one tidal period.

4. Simulation results

Owing to the large number of simulations done, only selected cases are presented here. Two series of simulations, A and B, were undertaken. They are for Coriolis frequencies $f = 6.7 \times 10^{-5} \, \text{s}^{-1}$ and $6.0 \times 10^{-5} \, \text{s}^{-1}$, respectively. Table 2 lists the parameters used for the two series. We define r_m as the part of the slope where $\alpha > 0.99\alpha_{max}$ and r_b as the x value of the location around which the beam is emitted. Here, α_{max} is the maximum value of the criticality parameter α, and x_c and x_{c0} are critical points. The slope is supercritical (subcritical) to the left (right) of x_c, and *vice versa* for x_{c0}. A stretch of the slope with $f_{eff} > \sigma_T$ is called a blocking region. The slope criticality α is undefined in blocking regions. The details on f_{eff}, γ, C and $C_{p(n)}$ for each case are plotted in figure 2.

f (s^{-1})	case	V_{max} (m s^{-1})	x_0 (km)	x_r (km)	r_m (km)	x_c (km)	x_{c0} (km)	r_b (km)
6.7×10^{-5}	A0	N/A			[5, 80]	N/A	N/A	20
	A1	1	50	60	blocking	45	N/A	55
	A2	1	36	60	blocking	31	N/A	41
	A3	1	64	60	blocking	59	0	69
	A4	1	92	60	blocking	77	7	80
	A5	−1	36	60	blocking	N/A	50	65
6.0×10^{-5}	B0	N/A			[5, 60]	N/A	N/A	20
	B1	1	41	40	[10, 14]	30	3	35
	B2	0.5	30	40	[8, 11]	N/A	N/A	25
	B3	−1	23	40	[47, 52]	53	31	53
	B4	−0.5	30	40	[42, 47]	N/A	N/A	45

Table 2. Parameters in A and B series. Here, V_{max}, x_0 and x_r are maximum velocity, the centre and the width of the current. Additionally, r_m is the part of the slope where $\alpha > 0.99\alpha_{max}$, x_c and x_{c0} are critical points, and r_b is the x value of the location around which the beam is emitted.

4.1. *Scenario I: no current*

We begin with the simplest cases A0 and B0 for which there are no background currents (magenta solid lines in figure 2). These provide a reference for cases with currents. The shelf slope lies between 0 and 81 (55) km for the A (B) series. We can see a large transient behaviour in the time evolution of the conversion rate $\bar{C}$ (figures 2e,f and 3a,b). At the beginning of the simulations, the wave field needs time to adjust to the sudden onset of the tidal forcing. It takes approximately 10 and 5 tidal periods for A0 and B0 to reach a quasi-steady state. Here α is constant on the majority of the slope and ITs are generated along the whole slope. The bathymetry is smoothed out near the bottom, so α is small near the base at $x = 0$ and near the shelf break, and it has its maximum value at the centre of the slope. For these cases, r_m is approximately the region (5 km, shelf break $-$ 5 km). For both cases, IT beams are emitted from a neighbourhood of $r_b \approx 20$ km (figure 3g,h) approximately 100 m above the bottom (figure 3c,d). To the left of $r_b \approx 20$ km is a beam with c_g propagating to the base of the slope then reflecting up to the left, and to the right a more intense beam propagates to the upper right. The phase of the rightward beam propagates downward (figure 3e,f) and the energy goes upward until it hits the surface and gets reflected (figure 3g,h). The characteristic IT beam path shown in green (figure 3c,d) is in general calculated using a ray-tracing technique although in the absence of a background current, they are straight lines. The beam energy continues to propagate onshore while being reflected by the surface and bottom. The beams generated near r_m are a common feature in all of our simulations, and it is related to positive conversion C_p. Each time the beam reflects, the sign of the conversion $\bar{C}$ changes (figure 3a,b).

4.2. *Scenario II: no critical point*

We include a current $V(x)$ with relatively small V_x so that $\alpha < 1$ everywhere. We consider cases B2 and B4, which only differ in the sign of V_{max} (blue dashed and black dashed lines in figure 2b,d,f,h). Unlike the cases A0 and B0, the slope criticality α here varies along the slope owing to the presence of the current. In B2 (positive current), α is increased (decreased) to the left (right) of the current centre x_0, with α reaching its maximum near the bottom at $r_m \approx 10$ km and its minimum is at $x \approx 50$ km. Two beams emanate from
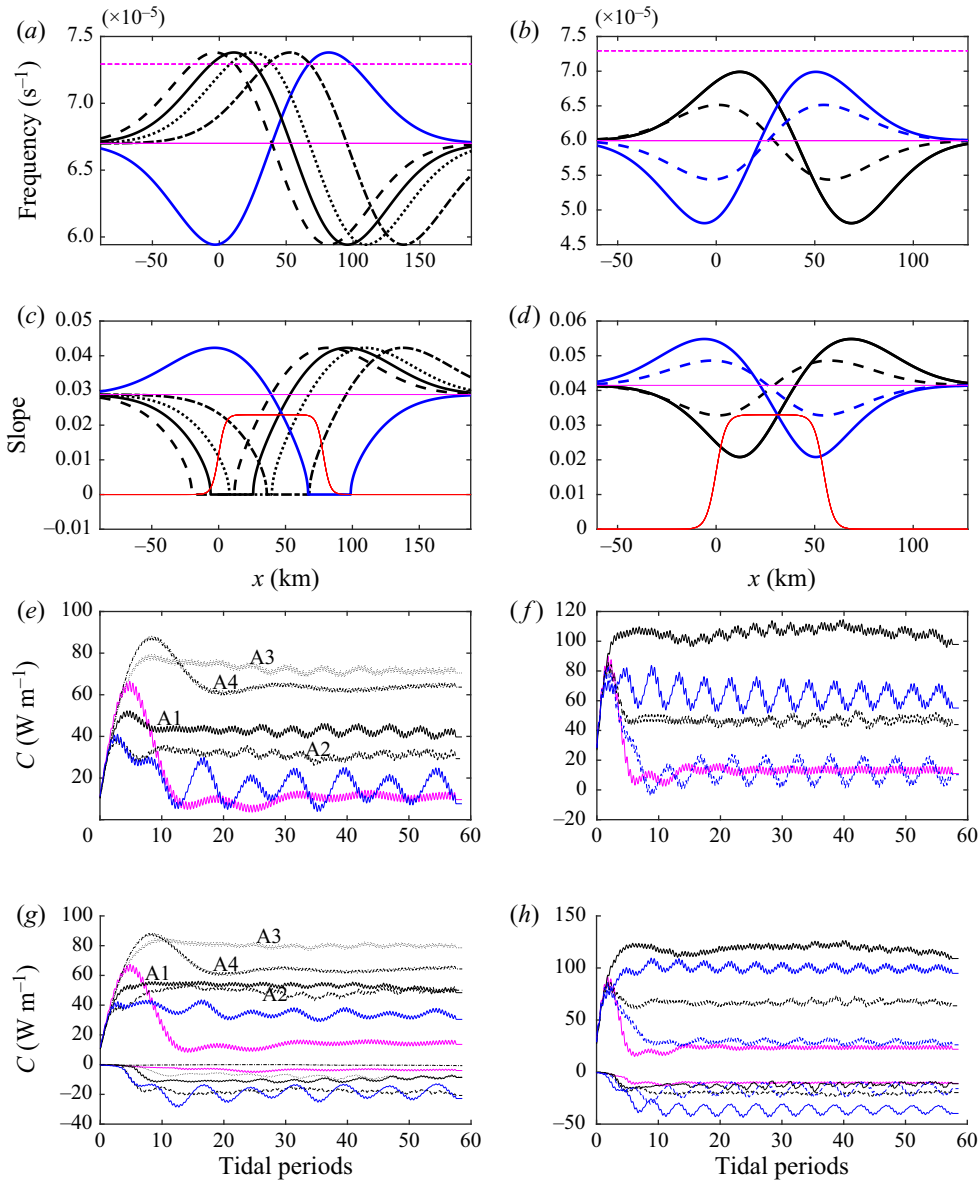
932 A55-8

Figure 2. (*a,c,e,g*) A series (magenta, black, black dashed, black dotted, black dash–dotted, blue) = (A0, A1, A2, A3, A4, A5). (*b,d,f,h*) B series (magenta solid, black, black dashed, blue, blue dashed) = (B0, B1, B2, B3, B4). (*a,b*) Effective frequencies. Magenta dashed (solid) line is σ_T (*f*). (*c,d*) Slope of IT characteristics γ. The red line is the bathymetric slope. (*e,f*) Total conversion rates C. (*g,h*) C_p and C_n.

$r_b \approx 25$ km (figure 4*c,g*). This difference in the *x*-location between beam emission and α_{max} (r_b and r_m) is presumably owing to the strengthening of the barotropic current with decreasing water depth. To the right of $r_b \approx 25$ km, the phase of the beam propagating downwards (figure 4*f*) indicates that energy propagates upwards (figure 4*h*). Note the slope of the beam is curved owing to the varying f_{eff}. The beam is emitted from a location similar to that in case B0 but the slope is closer to critical with $\alpha_{max} = 0.97$. As a result, the total conversion rate C in B2 is larger than in case B0 (black dashed line in figure 2*f*).
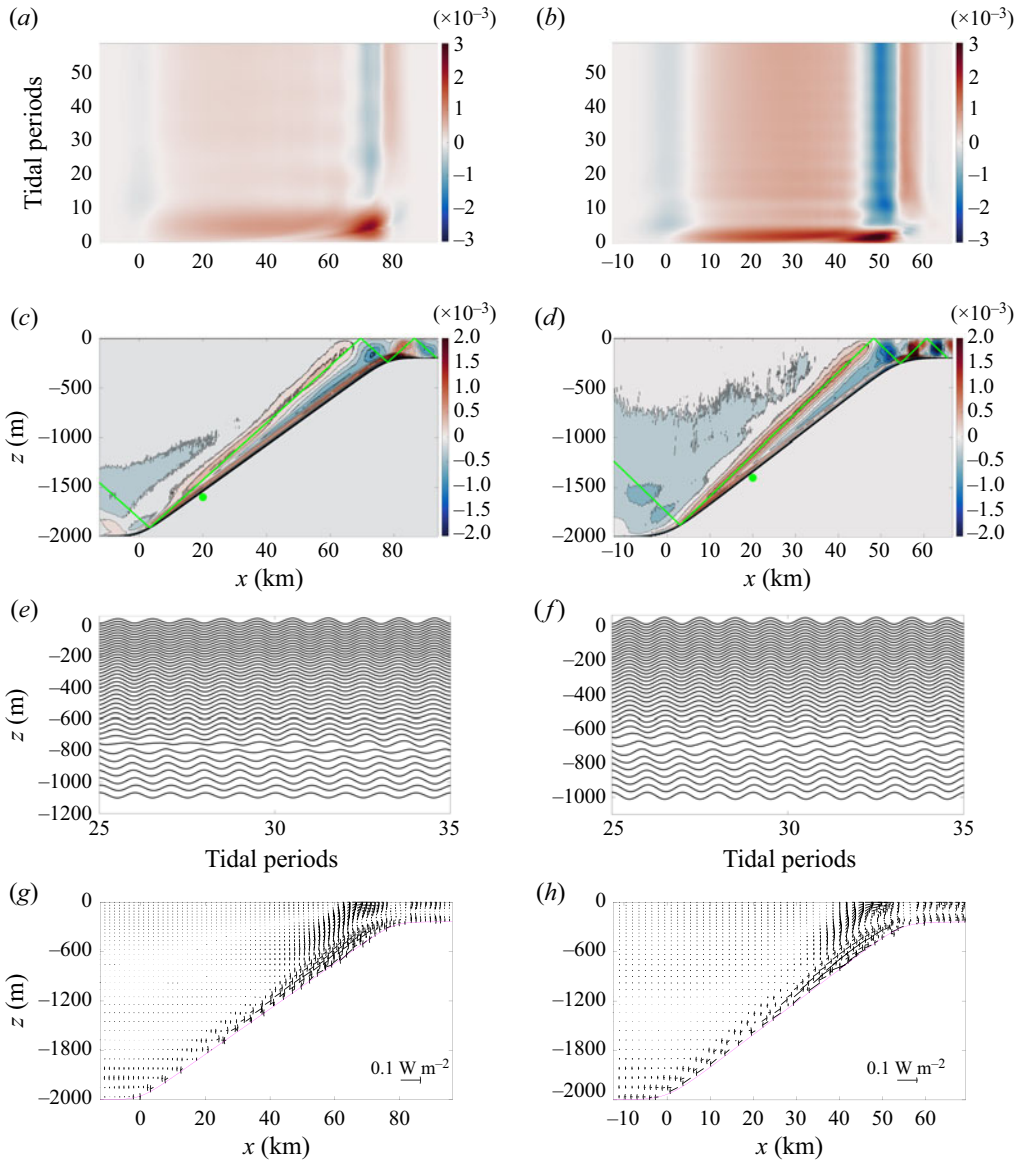
Figure 3. (*a,c,e,g*) Case A0. (*b,d,f,h*) Case B0. (*a,b*) Contour plot of the vertical integration of $\bar{C}$ (W m^{-2}) varying on the spatial and time scales. (*c,d*) Contour of the density perturbation ρ' at the end of 30 tidal periods. Green lines are the characteristics of IT beams. Green circles mark the location where the beam is emitted. (*e,f*) The horizontal baroclinic velocity u': (*e*) $x = 40$ km; (*f*) $x = 30$ km. (*g,h*) Energy flux $\langle (u', w')p' \rangle$.

In B4 with $V_{max} = -0.5$ m s^{-1}, $\alpha_{max} = 0.97$ occurs near the shelf break ($r_m \approx 45$ km) and it is smallest at $x \approx 15$ km. Three beams are emitted from the left and right of $r_b \approx r_m$ (figure 4*d*) Because the slope is subcritical on both sides of r_b, for the left downward propagating beam to be generated, the generation location must be above the slope. To verify this beam pattern, an extra simulation was conducted in which the water depth was increased by 400 m everywhere and the deep water barotropic current was increased so that the same barotropic tidal forcing is applied in the shallow water region. This makes
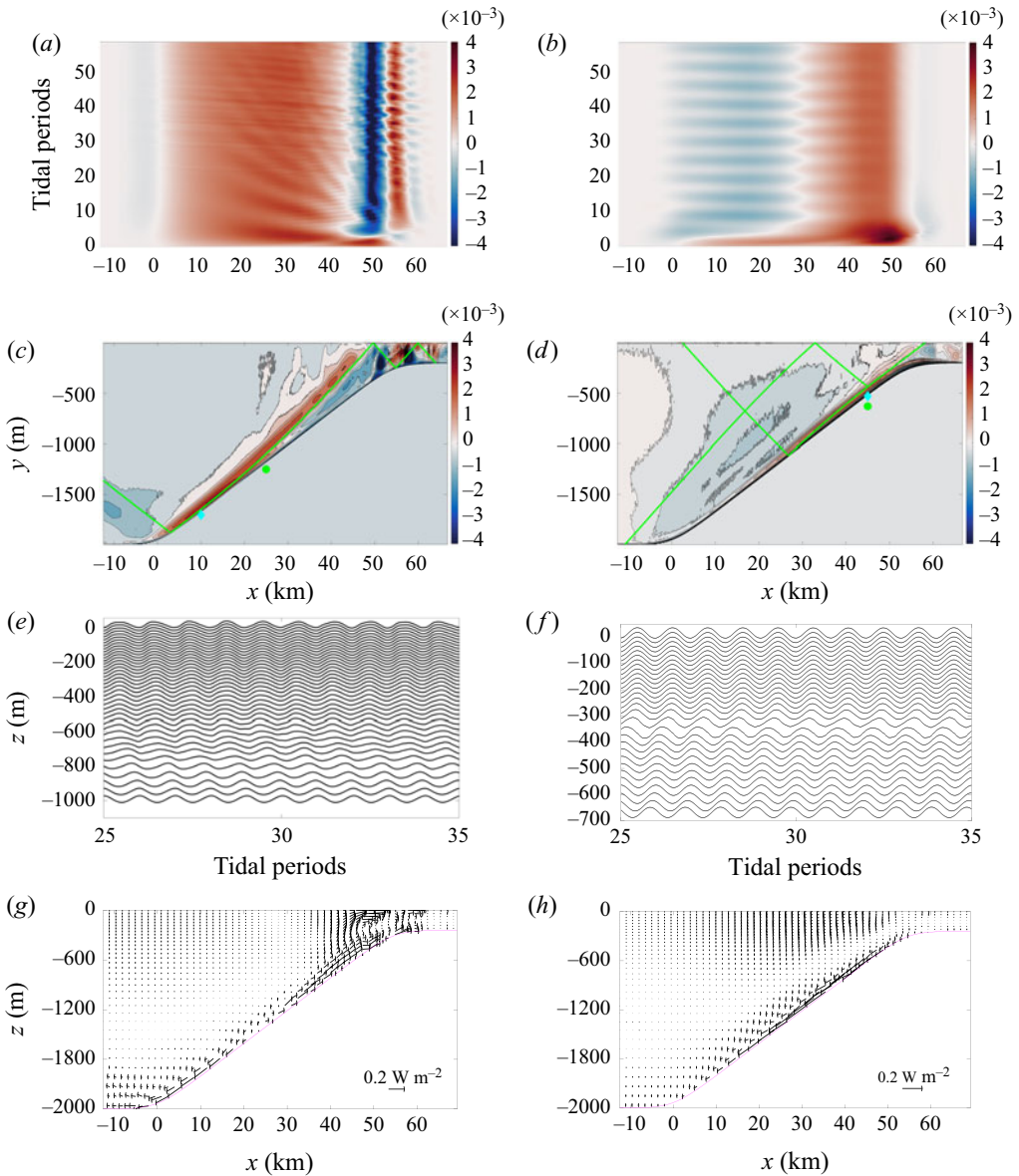
932 A55-10

Figure 4. Same as figure 3, except for case B2, with $V_{max} = 0.5 \, \text{m s}^{-1}$ (*a,c,e,g*) and case B4, with $V_{max} = -0.5 \, \text{m s}^{-1}$ (*b,d,f,h*). The cyan diamond marks r_m where α_{max} occurs. Green circles mark the location where the beam is emitted. Again, (*e*) $x = 40 \, \text{km}$, (*f*) $x = 30 \, \text{km}$.

the three IT beams more distinguishable. Details are omitted here. To the upper-left of r_b there is a wide beam, and to the lower-left and right of r_b there are two narrow beams. They each propagate onwards until hitting the surface/bottom, as illustrated in figure 4(*d,h*) for case B4. The upward phase propagation at $x = 30 \, \text{km}$ (figure 4*f*) confirms the downward c_g propagation. Owing to the different beam patterns in B4, the region of positive C_p (negative C_n) conversion (figure 4*b*) is different from those in cases B2 and B0. Here, C_p

932 A55-11

in B4 only exists for $x > 30$ km, which results a smaller total conversion rate C (dashed lines in figure 2*f,h*).

4.3. *Scenario III: No blocking + critical point*

We now double the current so that $\alpha \geq 1$ for some portion of the slope. We consider cases B1 with $V_{max} = 1$ m s^{-1} and B3 with $V_{max} = -1$ m s^{-1} (black and blue lines in figure 2*b,d,f,h*). There are two critical points in both cases.

In B1, one critical point $x_c = 30$ km lies in the middle of the slope and the other $x_{c0} = 3$ km is near the bottom. Between these two critical points, the slope is supercritical. There are two intense beams emanating from $r_b \approx 35$ km near x_c (figure 5*g*) but no beams near x_{c0}. This is because the slope is supercritical (subcritical) to the left (right) of x_c. However, the slope is subcritical (supercritical) to the left (right) of x_{c0}. No beams with a positive slope can be emitted from x_{c0}. Note the beam generation location r_b is up-slope of x_c owing to the strengthening of the barotropic current in the shallower water. An intense beam is emitted from the right of r_b and propagates upwards until it hits the surface at approximately $x = 53$ km (figure 5*c*). It gets reflected from the surface and keeps propagating onto the shelf while being reflected between the surface and the bottom. Analogously, the other intense beam emanates from the left of r_b with phase propagating upwards (figure 5*e*) and energy propagating downward (figure 5*g*) until it hits the bottom at approximately $x = -10$ km and gets reflected. The reflection location corresponds to the change of sign of $\bar{C}$ (figure 5*a*). The conversion rate $\bar{C}$ vanishes around $x = -10$ km because the bathymetry is flat and $W = 0$.

In case B3, the two critical points are at $x_c = 53$ km near the shelf break and $x_{c0} = 31$ km in the middle of the slope. The slope is subcritical (supercritical) to the left (right) of x_{c0}, while it is the other way around for x_c. As a result, beams can be generated at $r_b = x_c$ but not at x_{c0}. Three beams are emitted from $r_b = 53$ km (figure 5*d*). One beam emanates from the right of r_b and propagates to the upper right. Two beams emanate from the left of r_b. One of them propagates downwards until it reflects from the bathymetry at $x = 13$ km. The other beam propagates upwards and reflects from the surface at $x = 40$ km, where the reflected beam subsequently propagates downward until it hits the bottom at $x = -5$ km. The upward phase propagation at $x = 30$ km (figure 5*f*) confirms the downward energy propagation. Similar to case B4, a separate simulation with water depth increased by 400 m everywhere has been conducted to verify this beam pattern. Details are omitted here. The three beams emitted directly from r_b contribute to the positive conversion C_p, while their reflected beams contribute to the negative conversion C_n. The resulting conversion rate pattern $\bar{C}$ (figure 5*b*) is a combination of C_p and C_n.

Because strong generation occurs near the critical point x_c, B1 and B3 have the largest total conversion rate C in the B series (black and blue in figure 2*f*). However, owing to the different beam patterns, B3 has a much larger region of negative C_n than B1 (figure 5*a,b*). As a result, B3 has a smaller C than B1 (black and blue lines in figure 2*f,h*).

4.4. *Scenario IV: blocking near the bottom/shelf break*

We now consider a strong current such that $f_{eff} > \sigma_T$ along a stretch of the slope which we call a blocking region. Freely propagating internal waves do not exist in this region but tunnelling may occur. We analyse results from the A series with a focus on cases A1 ($V_{max} = 1$ m s^{-1}) and A5 ($V_{max} = -1$ m s^{-1}). For this series, the slope lies between $x = 0$ and 81 km.
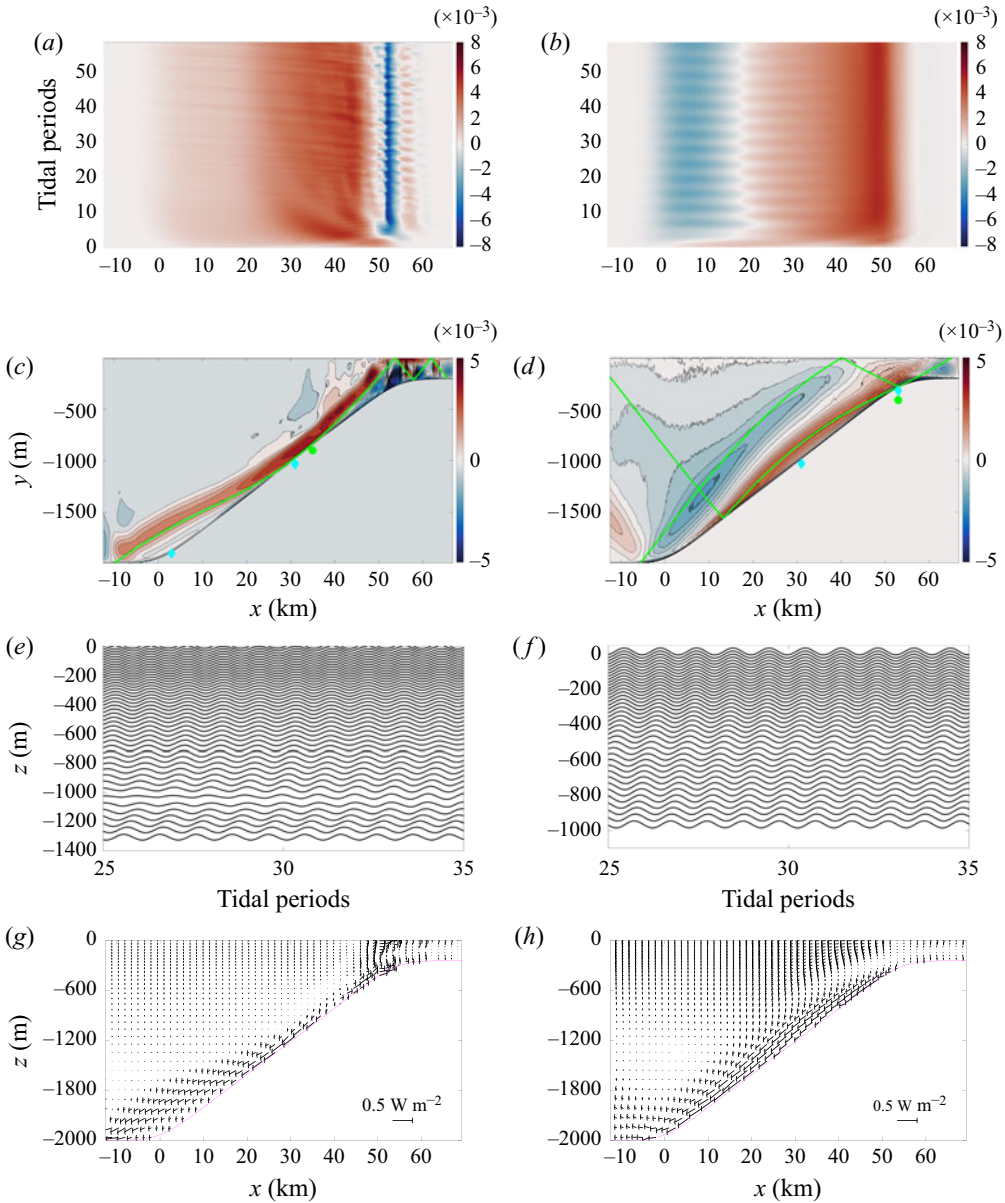
Figure 5. Same as figure 3, except for case B1 (*a,c,e,g*) and case B3 (*b,d,f,h*). The cyan diamonds mark the critical points x_c and x_{c0}. Green circles mark the location where the beam is emitted. Here, (*e*) $x = 20$ km, (*f*) $x = 30$ km.

In A1, there is a blocking region, $x \in [-5, 26]$ km, near the bottom of the slope (black line in figure 2*c*). There is a critical point at $x_c = 45$ km. To the left (right) of the critical point, the slope is supercritical (subcritical). Two strong narrow IT beams are emitted from $r_b \approx 55$ km near x_c (figure 6*c,g*). This pattern is similar to case B1. The difference is, here, the amplitude of the beams with tidal frequency σ_T decays quasi-exponentially to the left in the region -5 km $\leq x \leq 26$ km, where $f_{eff} > \sigma_T$. IT beams cannot be generated in this blocking region either. As a result, the conversion C in the blocking region is very
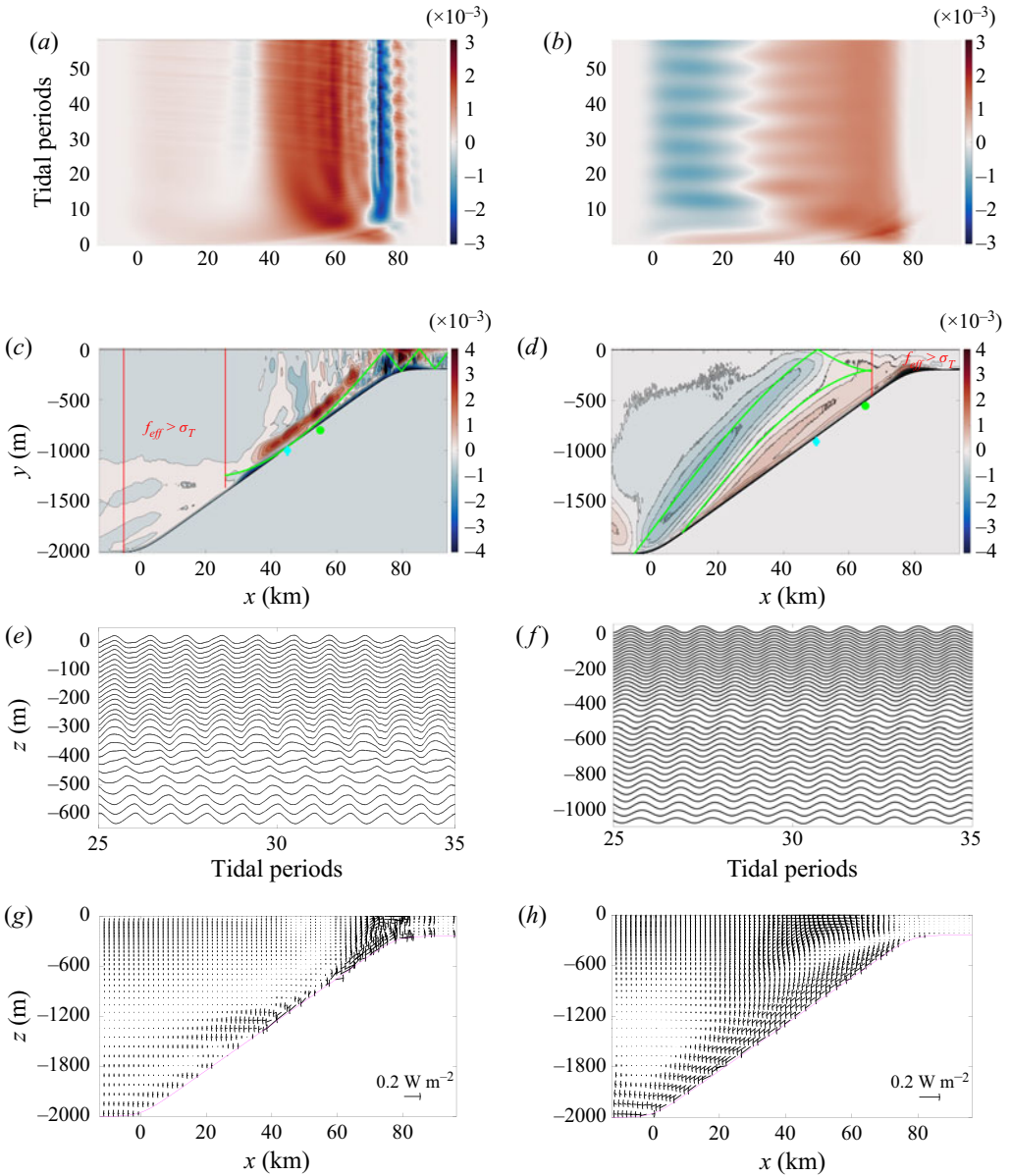
932 A55-13

Figure 6. Same as figure 3, except for case A1 (*a,c,e,g*) and case A5 (*b,d,f,h*). The cyan diamonds mark the critical points x_c and x_{c0}. Green circles mark the location where the beam is emitted. The red lines mark the edges of the blocking region. Here, (*e*) $x = 60$ km, (*f*) $x = 40$ km.

weak (figure 6*a*). For $x > 26$ km, the change of sign in C follows the IT beam reflection location.

Relative to A1, the centre of the current x_0 in cases A2, A3 and A4 is shifted up or down slope (figure 2*a*). There is a critical point x_c and a blocking region in each of these four cases. In general, the conversion rate C increases as x_c moves closer to the shelf break, because the barotropic tidal forcing reaches its maximum in the shallow water. In this case,
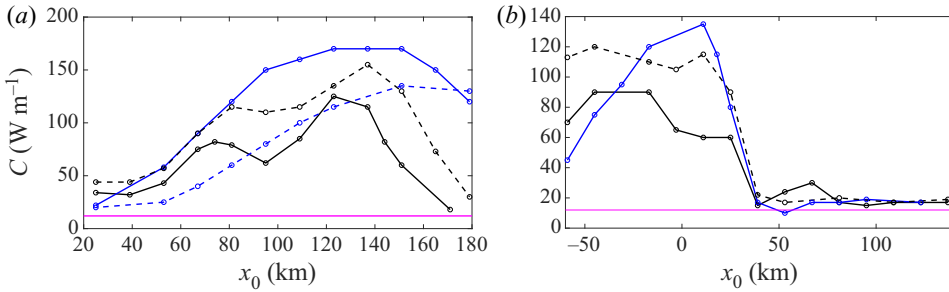
Figure 7. (*a*) Positive currents with $V_{max} = 1 \, \text{m s}^{-1}$. Current width x_r in (black solid, black dashed, blue solid, blue dashed) = (60 km, 75 km, 105 km, 160 km). (*b*) Negative currents. Here, V_{max} in (black solid, black dashed, blue) = $(-1 \, \text{m s}^{-1}, -1 \, \text{m s}^{-1}, -0.5 \, \text{m s}^{-1})$. x_r in (black solid, black dashed, blue) = (60 km, 75 km, 60 km). For both panels (*a,b*), $f = 6.7 \times 10^{-5} \, \text{s}^{-1}$. Shelf break is at 80 km. Magenta line is C without a current (case a0). Empty circles represent the numerical simulations.

we have $C(A3) > C(A1) > C(A2)$ (figure 2*c*). However, as the blocking region gets closer to the shelf break, C decreases explaining $C(A3) > C(A4)$.

In case A5, the current is negative and the blocking region, $x \in [65, 100]$ km, is near the shelf break (blue line in figure 2*c*). There is a critical point $x_{c0} = 50$ km, but no beams with positive slope can be emitted there because the slope is subcritical (supercritical) to the left (right) of x_{c0}. Because beams with tidal frequency cannot propagate upward owing to the blocking region and the slope is supercritical to the right of x_{c0}, two leftward propagating beams are generated approximately 300 m above the slope at $r_b \approx 65$ km, which is near the edge of the blocking region (figure 6*d,h*). One beam propagates downward and hits the slope at $x = 10$ km. The other beam propagates upwards and gets reflected at the surface $x = 50$ km. The upward phase propagation at $x = 40$ km (figure 6*f*) confirms the downward energy propagation. A separate simulation with water depth increased by 400 m everywhere has been conducted to confirm this beam pattern. Details are omitted here. The reflected (pre-reflected) beam contributes to the negative (positive) conversion C_n (C_p). The resulting conversion pattern is a combination of these two (figure 6*b*). This puts $C(A5)$ as the smallest among the five cases with currents in the A series.

5. Discussion and summary

How the current parameters influence the total conversion C is a complex problem. We illustrate it by conducting extra simulations and plotting the relation between C and the location of the current centre x_0 for different current widths (figure 7). When V_{max} is positive, $f_{eff} > f$ to the left of x_0 (deeper water) and $f_{eff} < f$ to the right of x_0 (shallower water) in the Northern Hemisphere where $f > 0$, which we have assumed throughout. As a consequence, IT characteristic slopes γ are reduced and the slope criticality α is increased to the left of x_0 while the opposite happens to the right of x_0. Here, C peaks when x_0 is placed in a position such that the portion of the slope that is near critical is maximized. In particular, the upper slope including the shelf break plays a dominant role because the tidal forcing there is the strongest. We can see this pattern in figure 7(*a*) with a small exception in the case of the narrowest current (black solid line): there are two local peaks when $(V_{max}, x_r) = (1 \, \text{m s}^{-1}, \, 60 \, \text{km})$. A blocking region exists to the left of x_0 for this case but not in the cases with wider currents because the velocity gradients are reduced as x_r increases. Note cases A1 to A4 are included in this line and we can refer to figure 2(*c*) for f_{eff} for these cases. When x_0 increases from 25 km near the bottom of the slope, C increases
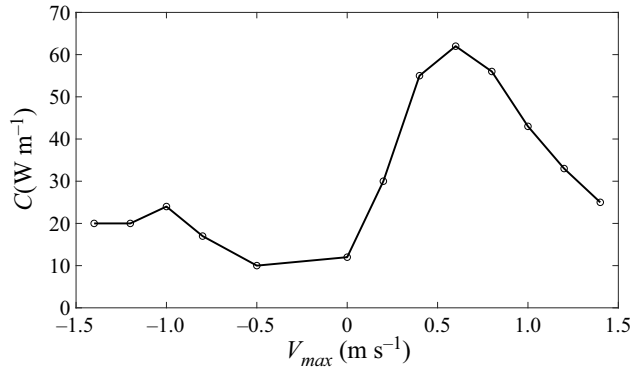
Figure 8. Conversion rate C as a function of V_{max}. Here, $f = 6.7 \times 10^{-5}\,\mathrm{s}^{-1}$, $(x_0, x_r) = (50\,\mathrm{km}, 60\,\mathrm{km})$.

because the critical point x_c is shifted closer to the shelf break with stronger tidal forcing. However as x_0 increases further, C decreases because the blocking region is moving to the shelf break where most of the generation occurs. This creates a first local peak at $x_0 = 75\,\mathrm{km}$ with the blocking region extending between 22 and 54 km. Subsequently, C increases again as the blocking region moves onto the shelf creating a second local peak at $x_0 = 123\,\mathrm{km}$. This second peak has a much larger C than the first peak because the slope criticality α is larger to the left of x_0. With x_0 on the shelf, only the left part of the current affects the value of α. If we increase the current width x_r, there is no blocking region and the maximum C occurs at a location with x_0 on the shelf. Cases with $x_r = 105\,\mathrm{km}$ (blue solid line) produce the largest C among the four lines. This is because the conversion rate C is determined by the two aspects of the slope criticality α, its magnitude and the portion of the slope where α is large. With a wider current, α is reduced but the region of the shelf slope with increased slope criticality increases.

Results for negative currents are shown in figure 7(*b*). As V_{max} changes sign, the behaviour of f_{eff} and α reverses too. The slope is closer to being critical to the right of x_0, meaning the peak of C occurs when the centre of the current is in deeper water (smaller x_0) than in the case of positive currents. Currents in the black solid line are stronger ($V_{max} = -1\,\mathrm{m\,s}^{-1}$) than those in the blue solid line ($V_{max} = -0.5\,\mathrm{m\,s}^{-1}$). However, the stronger currents have a generally smaller C owing to the presence of a blocking region (located to the right of x_0). Apart from these general statements, the exact magnitude of C is also affected by the contribution of C_p and C_n, which is predicted by the beam pattern. As a result, there is a sharp decrease in C as x_0 approaches 40 km.

The positive currents can increase the conversion rate C by up to 10 times (blue solid line in figure 7*a*) compared with case A0 (no current). The negative currents can also increase C but generally not so much as the positive currents do. This asymmetry can be seen using an example of how C varies with different V_{max} plotted in figure 8. The current width x_r and centre x_0 are the same as those of case A1. By reversing the sign of V_{max}, the variation of f_{eff} to the left and right of x_0 is reversed leading to different beam patterns. The two local peaks near $V_{max} = 0.6\,\mathrm{m\,s}^{-1}$ and $-1\,\mathrm{m\,s}^{-1}$ are a result of a blocking region from increasing $|V_{max}|$. As $|V_{max}|$ increases from 0, C first increases as a result of the rising slope criticality α. Then C decreases owing to the increasing size of the blocking region.

We summarize how the presence of a geostrophic barotropic current $V(x)$ affects the conversion rate.

932 A55-16

(i) The $V(x)$ changes the effective frequency from $f_{eff}^2 = f^2$ to $f_{eff}^2 = f^2 + f V_x$. This has a direct impact on the slope of the IT characteristics γ and the slope criticality $\alpha = s/\gamma$. It has been shown previously that α is a crucial factor in determining the total conversion C (e.g. Bell 1975; Baines 1982; Balmforth *et al.* 2002).

(ii) Because V_x is not a constant value, f_{eff} varies along the slope. This has a significant effect on IT beam generation location r_b and their propagation paths. When $f_{eff} < \sigma_T$, internal waves are generated everywhere along the slope. The intensity of the IT beams depends on the current, which also determines the beam generation location r_b. Here, r_m is defined as the part of the slope where $\alpha > 0.99\alpha_{max}$ and r_b is usually equivalent to or slightly larger than the upper bound of r_m because tidal forcing increases as the water depth decreases. With a slightly stronger current such that part of the slope is critical/supercritical, IT beams can be emitted near a critical point x_c if the slope is of the same sign as the slope of the beam and it is subcritical (supercritical) to the left (right) of x_c but not the other way around. With a strong current such that part of the slope acts as a blocking region where $f_{eff} > \sigma_T$, IT beams are emitted near a critical point and the conversion rate C becomes extremely small in the blocking region.

(iii) The change of sign in $\bar{C}$ corresponds to the IT beam reflection location. As a result, the total conversion rate $C = C_p + C_n$ is also strongly affected by the IT beam pattern, which depends on V_x.

In conclusion, the total conversion rate C is affected by a combination of three factors: slope criticality α, the size and location of the blocking region where ITs cannot be generated, and the IT beam pattern including where the beams are emitted and reflected, all of which can be varied by the geostrophic current V. In this paper, we assumed $f > 0$, i.e. the Northern Hemisphere, and K_1 diurnal tides as the forcing. Our work can be extended to the Southern Hemisphere by simply reversing the signs of f and V_{max}. It can also be applied to any other tidal constituents as long as f is close to the tidal frequency so that $\sigma_T^2 - f_{eff}^2 = \sigma_T^2 - f^2 - f V_x$ in (1.1) can vary significantly by varying V_x. This is easiest if $\sigma_T^2 - f^2$ is small. What matters is the dimensionless parameter $\tilde{f} = f/\sigma_T$. In our paper, $\tilde{f} \geq 0.82$. At latitudes far from critical, i.e. $f \ll \sigma_T$ and $\tilde{f} \ll 1$, the slope criticality will be modified by V_x but the effects are expected to be reduced. As a result, the conversion rate is modified but not as much as that of the near-critical latitudes.

Although we considered idealized cases that use a linear stratification and a symmetric barotropic current, the key point of this work is that the current changes f_{eff} which changes the conversion. This is unlikely to change in a more realistic setting. For example, with a varying $N(z)$ in the absence of a current, the IT beams will bend instead of following a straight line. However, the presence of a current would affect how the beam bends and the slope criticality in the same way that we have described in this paper. Including baroclinic currents is an important future problem of this research, because it introduces horizontal density gradients. Other important future avenues of this research are to incorporate asymmetric currents and more realistic bathymetry. The effects of background currents on PSI, which can occur at lower latitudes where $2f_{eff} \approx \sigma_T$ is the subject of ongoing work.

Declaration of interests. The authors report no conflict of interest.

Author ORCIDs.

Yangxin He https://orcid.org/0000-0002-9470-2550;

Kevin G. Lamb https://orcid.org/0000-0003-3804-6525.

REFERENCES

BAINES, P.G. 1973 The generation of internal tides by flat-bump topography. *Deep Sea Res.* **20**, 179–205.

BAINES, P.G. 1982 On internal tide generation models. *Deep Sea Res.* A **29** (3), 307–338.

BALMFORTH, N.J., IERLEY, G.R. & YOUNG, W.R. 2002 Tidal conversion by subcritical topography. *J. Phys. Oceanogr.* **32** (10), 2900–2914.

BELL, T.H. 1975 Topographically generated internal waves in the open ocean. *J. Geophys. Res.* **80** (3), 320–327.

CACCHIONE, D.A., PRATSON, L.F. & OGSTON, A.S. 2002 The shaping of continental slopes by internal tides. *Science* **296** (5568), 724–727.

CHAVANNE, C., FLAMENT, P., LUTHER, D. & GURGEL, K.W. 2010 The surface expression of semidiurnal internal tides near a strong source at Hawaii. Part II: interactions with mesoscale currents. *J. Phys. Oceanogr.* **40** (6), 1180–1200.

CHUANG, W.-S. & WANG, D.-P. 1981 Effects of density front on the generation and propagation of internal tides. *J. Phys. Oceanogr.* **11** (10), 1357–1374.

CRAIG, P.D. 1987 Solutions for internal tidal generation over coastal topography. *J. Mar. Res.* **45** (1), 83–105.

DONG, J., ROBERTSON, R., DONG, C., HARTLIPP, P.S., ZHOU, T., SHAO, Z., LIN, W., ZHOU, M. & CHEN, J. 2019 Impacts of mesoscale currents on the diurnal critical latitude dependence of internal tides: a numerical experiment based on Barcoo Seamount. *J. Geophys. Res.: Oceans* **124** (4), 2452–2471.

ECKART, C. 1961 Internal waves in the ocean. *Phys. Fluids* **4** (7), 791–799.

GARRETT, C. & KUNZE, E. 2007 Internal tide generation in the deep ocean. *Annu. Rev. Fluid Mech.* **39**, 57–87.

GERKEMA, T. 2002 Application of an internal tide generation model to baroclinic spring-neap cycles. *J. Geophys. Res.: Oceans* **107** (C9), 3124.

GERKEMA, T., LAM, F.-P.A. & MAAS, L.R.M. 2004 Internal tides in the Bay of Biscay: conversion rates and seasonal effects. *Deep-Sea Res.* II **51** (25–26), 2995–3008.

HALL, M.M. & BRYDEN, H.L. 1982 Direct estimates and mechanisms of ocean heat transport. *Deep Sea Res.* A **29** (3), 339–359.

HOLLOWAY, P.E. 1996 A numerical model of internal tides with application to the Australian North West Shelf. *J. Phys. Oceanogr.* **26** (1), 21–37.

HOLLOWAY, P.E., CHATWIN, P.G. & CRAIG, P. 2001 Internal tide observations from the Australian North West Shelf in summer 1995. *J. Phys. Oceanogr.* **31** (5), 1182–1199.

HOLLOWAY, P.E. & MERRIFIELD, M.A. 1999 Internal tide generation by seamounts, ridges, and islands. *J. Geophys. Res.: Oceans* **104** (C11), 25937–25951.

JONES, W.L. 1970 A theory for quasi-periodic oscillations observed in the ionosphere. *J. Atmos. Terrest. Phys.* **32** (9), 1555–1566.

KANG, D. & FRINGER, O. 2012 Energetics of barotropic and baroclinic tides in the Monterey Bay area. *J. Phys. Oceanogr.* **42** (2), 272–290.

KHATIWALA, S. 2003 Generation of internal tides in an ocean of finite depth: analytical and numerical calculations. *Deep-Sea Res.* I **50** (1), 3–21.

KOLOMOITSEVA, E.M. & CHERKESOV, L.V. 1999 Generation of internal waves in the region of a bottom ridge with continuously varying height. *Phys. Oceanogr.* **9** (6), 433–443.

KUNZE, E. 1985 Near-inertial wave propagation in geostrophic shear. *J. Phys. Oceanogr.* **15** (5), 544–565.

KUNZE, E., ROSENFELD, L.K., CARTER, G.S. & GREGG, M.C. 2002 Internal waves in Monterey submarine canyon. *J. Phys. Oceanogr.* **32** (6), 1890–1913.

KURAPOV, A.L., ALLEN, J.S. & EGBERT, G.D. 2010 Combined effects of wind-driven upwelling and internal tide on the continental shelf. *J. Phys. Oceanogr.* **40** (4), 737–756.

LAMB, K.G. & KIM, J. 2012 Conversion of barotropic tidal energy to internal wave energy over a shelf slope for a linear stratification. *Cont. Shelf Res.* **33**, 69–88.

LEGG, S. & HUIJTS, K.M.H. 2006 Preliminary simulations of internal waves and mixing generated by finite amplitude tidal flow over isolated topography. *Deep-Sea Res.* II **53** (1–2), 140–156.

LI, Q., MAO, X., HUTHNANCE, J., CAI, S. & KELLY, S. 2019 On internal waves propagating across a geostrophic front. *J. Phys. Oceanogr.* **49** (5), 1229–1248.

LIEN, R.-C. & GREGG, M.C. 2001 Observations of turbulence in a tidal beam and across a coastal ridge. *J. Geophys. Res.: Oceans* **106** (C3), 4575–4591.

LLEWELLYN SMITH, S.G. & YOUNG, W.R. 2002 Conversion of the barotropic tide. *J. Phys. Oceanogr.* **32** (5), 1554–1566.

LUECK, R.G. & MUDGE, T.D. 1997 Topographically induced mixing around a shallow seamount. *Science* **276** (5320), 1831–1833.

MARSHALL, J., ADCROFT, A., HILL, C., PERELMAN, L. & HEISEY, C. 1997 A finite-volume, incompressible Navier stokes model for studies of the ocean on parallel computers. *J. Geophys. Res.: Oceans* **102** (C3), 5753–5766.

MARTIN, J.P., RUDNICK, D.L. & PINKEL, R. 2006 Spatially broad observations of internal waves in the upper ocean at the Hawaiian ridge. *J. Phys. Oceanogr.* **36** (6), 1085–1103.

MERRIFIELD, M.A., HOLLOWAY, P.E. & JOHNSTON, T.M.S. 2001 The generation of internal tides at the Hawaiian Ridge. *Geophys. Res. Lett.* **28** (4), 559–562.

MONSERRAT, S. & THORPE, A.J. 1996 Use of ducting theory in an observed case of gravity waves. *J. Atmos. Sci.* **53** (12), 1724–1736.

MOOERS, C.N.K. 1975 Several effects of a baroclinic current on the cross-stream propagation of inertial-internal waves. *Geophys. Astrophys. Fluid Dyn.* **6** (3), 245–275.

MUNK, W. & WUNSCH, C. 1998 Abyssal recipes II: energetics of tidal and wind mixing. *Deep-Sea Res* I **45** (12), 1977–2010.

MUNROE, J.R. & LAMB, K.G. 2005 Topographic amplitude dependence of internal wave generation by tidal forcing over idealized three-dimensional topography. *J. Geophys. Res.: Oceans* **110** (C2), CO2001.

NEW, A.L. & PINGREE, R.D. 1992 Local generation of internal soliton packets in the central Bay of Biscay. *Deep Sea Res.* A **39** (9), 1521–1534.

NIWA, Y. & HIBIYA, T. 2004 Three-dimensional numerical simulation of m2 internal tides in the East China Sea. *J. Geophys. Res.: Oceans* **109**, C04027.

NIWA, Y. & HIBIYA, T. 2011 Estimation of baroclinic tide energy available for deep ocean mixing based on three-dimensional global numerical simulations. *J. Oceanogr.* **67** (4), 493–502.

NIWA, Y. & HIBIYA, T. 2014 Generation of baroclinic tide energy in a global three-dimensional numerical model with different spatial grid resolutions. *Ocean Model.* **80**, 59–73.

NYCANDER, J. 2006 Tidal generation of internal waves from a periodic array of steep ridges. *J. Fluid Mech.* **567**, 415–432.

PACANOWSKI, R.C. & PHILANDER, S.G.H. 1981 Parameterization of vertical mixing in numerical models of tropical oceans. *J. Phys. Oceanogr.* **11** (11), 1443–1451.

PÉTRÉLIS, F., SMITH, S.L. & YOUNG, W.R. 2006 Tidal conversion at a submarine ridge. *J. Phys. Oceanogr.* **36** (6), 1053–1071.

POLZIN, K.L., TOOLE, J.M., LEDWELL, J.R. & SCHMITT, R.W. 1997 Spatial variability of turbulent mixing in the abyssal ocean. *Science* **276** (5309), 93–96.

POWELL, B.S., JANEKOVIĆ, I., CARTER, G.S. & MERRIFIELD, M.A. 2012 Sensitivity of internal tide generation in Hawaii. *Geophys. Res. Lett.* **39**, L10606.

RAINVILLE, L. & PINKEL, R. 2004 Observations of energetic high-wavenumber internal waves in the Kuroshio. *J. Phys. Oceanogr.* **34** (7), 1495–1505.

RAINVILLE, L. & PINKEL, R. 2006 Propagation of low-mode internal waves through the ocean. *J. Phys. Oceanogr.* **36** (6), 1220–1236.

RICHET, O., MULLER, C. & CHOMAZ, J.-M. 2017 Impact of a mean current on the internal tide energy dissipation at the critical latitude. *J. Phys. Oceanogr.* **47** (6), 1457–1472.

SCHAFSTALL, J., DENGLER, M., BRANDT, P. & BANGE, H. 2010 Tidal-induced mixing and diapycnal nutrient fluxes in the Mauritanian upwelling region. *J. Geophys. Res.: Oceans* **115**, C10014.

SIMMONS, H.L. & ALFORD, M.H. 2012 Simulating the long-range swell of internal waves generated by ocean storms. *Oceanography* **25** (2), 30–41.

SIMMONS, H.L., HALLBERG, R.W. & ARBIC, B.K. 2004 Internal wave generation in a global baroclinic tide model. *Deep-Sea Res.* II **51** (25–26), 3043–3068.

SMAGORINSKY, J. 1993 *Large Eddy Simulation of Complex Engineering and Geophysical Flows*. Cambridge University Press.

ST. LAURENT, L. & GARRETT, C. 2002 The role of internal tides in mixing the deep ocean. *J. Phys. Oceanogr.* **32** (10), 2882–2899.

ST. LAURENT, L., STRINGER, S., GARRETT, C. & PERRAULT-JONCAS, D. 2003 The generation of internal tides at abrupt topography. *Deep-Sea Res.* I **50** (8), 987–1003.

STAMMER, D., *et al.* 2014 Accuracy assessment of global barotropic ocean tide models. *Rev. Geophys.* **52** (3), 243–282.

STASHCHUK, N., VLASENKO, V., HOSEGOOD, P. & NIMMO-SMITH, W.A.M. 2017 Tidally induced residual current over the Malin sea continental slope. *Cont. Shelf Res.* **139**, 21–34.

SUTHERLAND, B.R. & YEWCHUK, K. 2004 Internal wave tunnelling. *J. Fluid Mech.* **511**, 125–134.

TOOLE, J.M., SCHMITT, R.W., POLZIN, K.L. & KUNZE, E. 1997 Near-boundary mixing above the flanks of a midlatitude seamount. *J. Geophys. Res.: Oceans* **102** (C1), 947–959.

VIC, C., GARABATO, A.C.N., GREEN, J.A.M., WATERHOUSE, A.F., ZHAO, Z., MELET, A., DE LAVERGNE, C., BUIJSMAN, M.C. & STEPHENSON, G.R. 2019 Deep-ocean mixing driven by small-scale internal tides. *Nat. Commun.* **10** (1), 2099.

VLASENKO, V., STASHCHUK, N. & HUTTER, K. 2005 *Baroclinic Tides: Theoretical Modeling and Observational Evidence*. Cambridge University Press.

WHITT, D.B. & THOMAS, L.N. 2013 Near-inertial waves in strongly baroclinic currents. *J. Phys. Oceanogr.* **43** (4), 706–725.

WUNSCH, C. & FERRARI, R. 2004 Vertical mixing, energy, and the general circulation of the oceans. *Annu. Rev. Fluid Mech.* **36**, 281–314.

XING, J. & DAVIES, A.M. 1998 A three-dimensional model of internal tides on the Malin-Hebrides shelf and shelf edge. *J. Geophys. Res.: Oceans* **103** (C12), 27821–27847.

ZILBERMAN, N.V., BECKER, J.M., MERRIFIELD, M.A. & CARTER, G.S. 2009 Model estimates of M2 internal tide generation over mid-atlantic ridge topography. *J. Phys. Oceanogr.* **39** (10), 2635–2651.